Supplement of Solid Earth, 12, 79–93, 2021
https://doi.org/10.5194/se-12-79-2021-supplement

Solid Earth
Open Access

Supplement of

Effects of basal drag on subduction dynamics from 2D numerical models

Lior Suchoy et al.

Correspondence to: Lior Suchoy (l.suchoy17@imperial.ac.uk)

This supplement comprises three main sections and references section:

S1. Governing equations and rheology calculations for the numerical models

S2. Illustration of the evolution of all models discussed in the main text

S3. Cenozoic subduction zone parameters

S1. Governing equations and rheology calculations for the numerical models

We solve flow for incompressible Stokes fluid, under the Boussinesq approximation, assuming mass, momentum and energy conservation equations:

$$\partial_i u_i = 0 \tag{S1.1}$$

$$\partial_i \sigma_{ij} + \Delta\rho g_j = 0 \tag{S1.2}$$

$$\frac{\partial T}{\partial t} + u_i \partial_i T - \kappa \partial_i^2 T = 0 \tag{S1.3}$$

where u is the velocity, σ is the stress tensor, g is gravity, T is temperature, κ is the thermal diffusivity and $\Delta\rho = -\alpha\rho_s \Delta T$ is the density difference due to temperature, with α the coefficient of thermal expansion, ρ_s the reference (surface) mantle density and ΔT the difference in temperature from the surface.

Viscosity is therefore the ratio of deviatoric stress to strain rate:

$$\mu = \frac{\tau_{ij}}{2\dot{\varepsilon}_{ij}} = \frac{\sigma_{ij} + P\delta_{ij}}{2\dot{\varepsilon}_{ij}} \tag{S1.4}$$

where τ is the deviatoric stress, $\dot{\varepsilon}$ is the strain rate, P is the dynamic pressure and δ_{ij} is the delta function. The viscosity is calculated in our models using:

$$\mu = \left(\frac{1}{\mu_{diff}} + \frac{1}{\mu_{disl}} + \frac{1}{\mu_y} + \frac{1}{\mu_{Pie}}\right)^{-1} \tag{S1.5}$$

where μ_{diff}, μ_{disl}, μ_y and μ_{Pie} are the viscosities calculated using diffusion creep, dislocation creep, yielding mechanism and simplified Pierels creep, respectively. The viscosities derived from diffusion, dislocation and Pierels creep are calculated using the generalised equation:

$$\mu_{diff\backslash disl\backslash Pie} = A^{\frac{-1}{n}} \exp\left(\frac{E + P_l V}{nRT_{ad}}\right) \dot{\varepsilon}_{II}^{\frac{1-n}{n}} \tag{S1.6}$$

$$P_l = \rho g D \tag{S1.7}$$

where A is a prefactor, n is the stress exponent, E and V are the activation energy and volume, respectively, P_l is the lithostatic pressure, R the gas constant, $\dot{\varepsilon}_{II}$ is the second invariant of the strain rate tensor and D is the depth. T_{ad} is the temperature adjusted with an adiabatic gradient of 0.5°K/km in the upper mantle and 0.3°K/km in the lower mantle (Fowler, 2005). The yielding mechanism is calculated as:

$$\mu_y = \frac{\tau_y}{2\dot{\varepsilon}_{II}} = \frac{\min(\tau_s + f_c P_l, \tau_{y\,max})}{2\dot{\varepsilon}_{II}} \quad \text{(S1.8)}$$

where τ_y is the yield stress, τ_s is the surface yield stress, f_c is the friction coefficient and $\tau_{y\,max}$ is the maximum yield stress. The viscosity field is capped by both minimum and maximum values. The yielding viscosity is adjusted within the weak decoupling layer by applying a different friction coefficient:

$$\mu_{y\,weak} = \frac{\min(\tau_s + f_{c\,weak} P_l, \tau_{y\,max})}{2\dot{\varepsilon}_{II}} \quad \text{(S1.9)}$$

The initial temperature field in the lithosphere is calculated using the half-space cooling equation from Turcotte and Schubert (2002):

$$T = T_s + \Delta T \cdot \mathrm{erf}\left(\frac{D}{2\sqrt{\kappa t_{age}}}\right) \quad \text{(S1.10)}$$

where T_s is the surface temperature and t_{age} is the age.

Quantity	Symbol	Units	Value		
			UM (Reference) [a]	UM (modified self-consistent) [b]	LM [a]
Gravity	g	$m \cdot s^{-2}$	9.8		
Thermal expansivity coefficient	α	K^{-1}	$3.0 \cdot 10^{-5}$		
Thermal diffusivity	κ	$m^2 \cdot s^{-1}$	10^{-6}		
Reference (surface) density	ρ_s	$kg \cdot m^{-3}$	3300.0		
Cold, surface temperature	T_s	K	273.0		
Hot, mantle temperature	T_m		1573.0		
Gas constant	R	$J \cdot K^{-1} \cdot mol^{-1}$	8.3145		
Maximum viscosity (Strong Lithosphere model)	μ_{max}	$Pa \cdot s$	10^{26}		
Maximum viscosity (Reference and all other models)			10^{25}		
Minimum viscosity	μ_{min}		10^{18}		
Diffusion Creep					
Activation energy	E	$J \cdot mol^{-1}$	$300.0 \cdot 10^3$	$335.0 \cdot 10^3$	$200.0 \cdot 10^3$
Activation volume	V	$m^3 \cdot mol^{-1}$	$4.0 \cdot 10^{-6}$	$5.0 \cdot 10^{-6}$	$1.5 \cdot 10^{-6}$
Pre-factor	A	$Pa^{-n} \cdot s^{-1}$	$3.0 \cdot 10^{-11}$	$1.5 \cdot 10^{-9}$	$6.0 \cdot 10^{-17}$
Stress exponent	n		1.0		
Dislocation Creep (UM)					
Activation energy	E	$J \cdot mol^{-1}$	$540.0 \cdot 10^3$	$472.0 \cdot 10^3$	$300.0 \cdot 10^3$
Activation volume	V	$m^3 \cdot mol^{-1}$	$12.0 \cdot 10^{-6}$	$11.0 \cdot 10^{-6}$	$2.0 \cdot 10^{-6}$
Pre-factor	A	$Pa^{-n} \cdot s^{-1}$	$5.0 \cdot 10^{-16}$	$1.34 \cdot 10^{-17}$	10^{-42}
Stress exponent	n		3.5	3.472	3.5
Peierls Creep (UM)					
Activation energy	E	$J \cdot mol^{-1}$	$540.0 \cdot 10^3$	$540.0 \cdot 10^3$	$300.0 \cdot 10^3$
Activation volume	V	$m^3 \cdot mol^{-1}$	$10.0 \cdot 10^{-6}$	$10.0 \cdot 10^{-6}$	$2.0 \cdot 10^{-6}$
Pre-factor	A	$Pa^{-n} \cdot s^{-1}$	10^{-150}	10^{-145}	10^{-300}
Stress exponent	n		20.0		
Yield Strength Law					
Surface yield strength	τ_s	MPa	2.0		
Friction coefficient	f_c		0.2		
Friction coefficient (decoupling layer)	$f_{c\ weak}$		0.02	0.07	0.02
Maximum yield strength	$\tau_{y\ max}$	MPa	10,000		

Table S1-1: Physical and rheological parameters of all models, following the model set-up used by Garel et al., 2014. (a) Activation parameters and stress exponent are consistent with experimental data on olivine (e.g., Karato and Wu, 1993; Hirth and Kohlstedt, 1995; Ranalli, 1995; Hirth and Kohlstedt, 2003; Korenaga and Karato, 2008). Lower mantle pre-factor value for dislocation and Peierls creep are set at a low value to ensure diffusion creep-controlled viscosity in the lower mantle (in accordance with eq. S1.5). (b) Upper mantle values for the modified self-consistent models were determined using optimisation method described in Maunder et al., 2016. See main text for further details.

S2. Illustration of the evolution of all models discussed in the main text

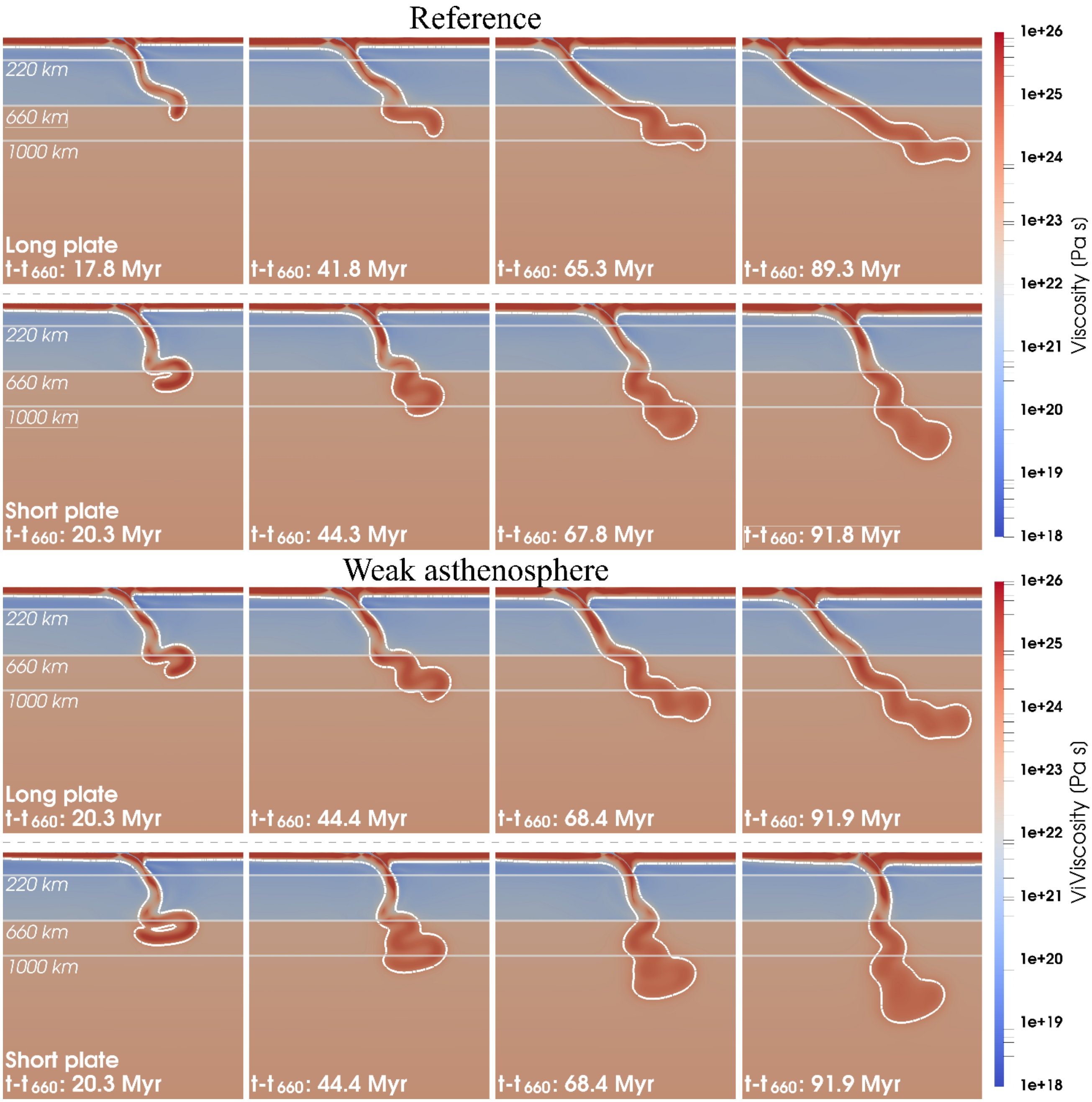

Figure S2-1: Viscosity field evolution at various times, similar to Fig. 3, for the long-plate case (top row of each model) and short-plate case (bottom row of each model) for all models. White contour marks the 1100 °C isotherm used as the outline of the lithosphere. The vertical and horizontal scales are identical and only part of the full model domain is shown. t-t660 indicates the time since the initial interaction of the slab with the ULMB. Grey lines mark 220 km, 660 km (ULMB) and 1000 km depths.

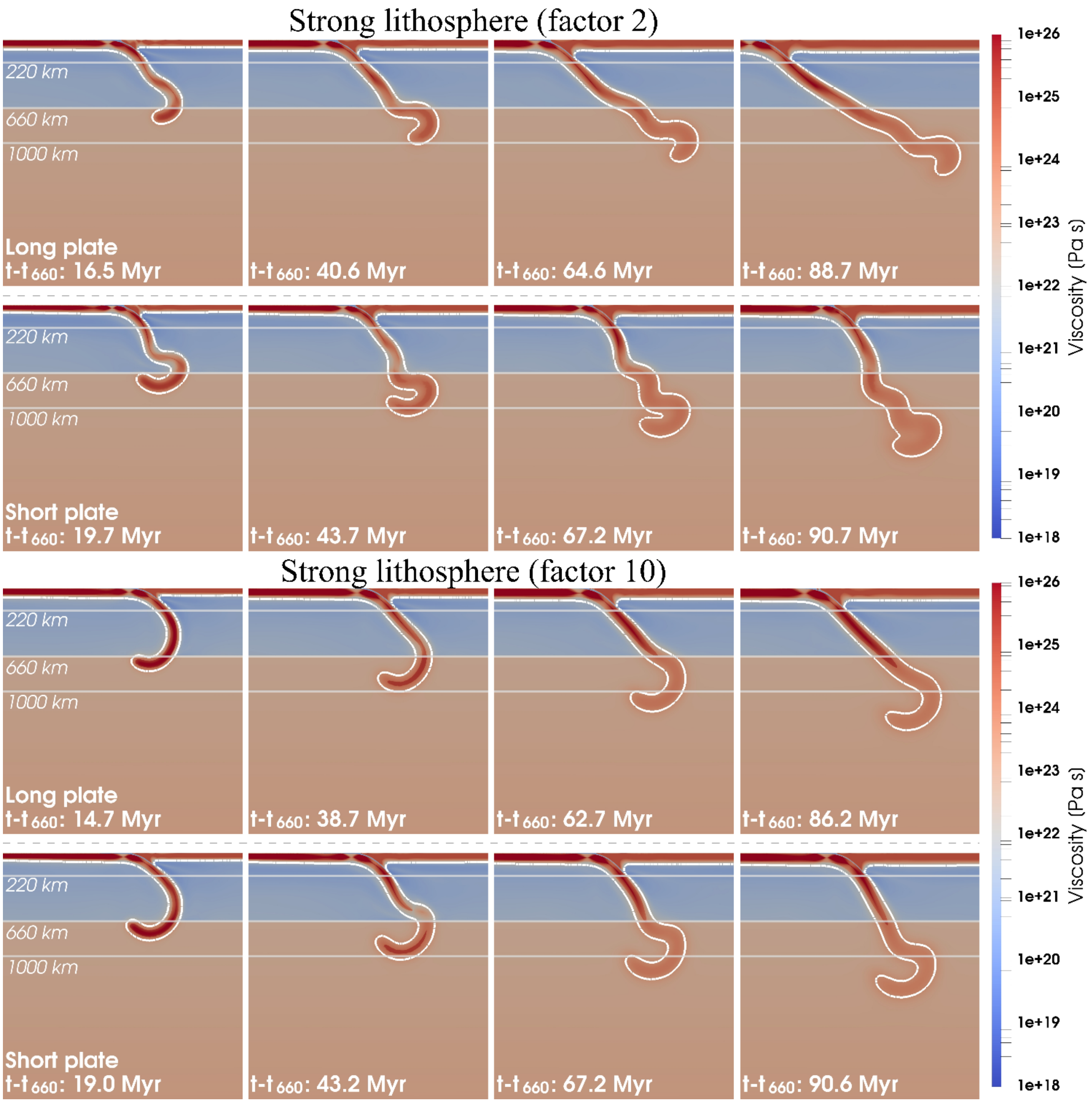

Figure S2-1 (continued)

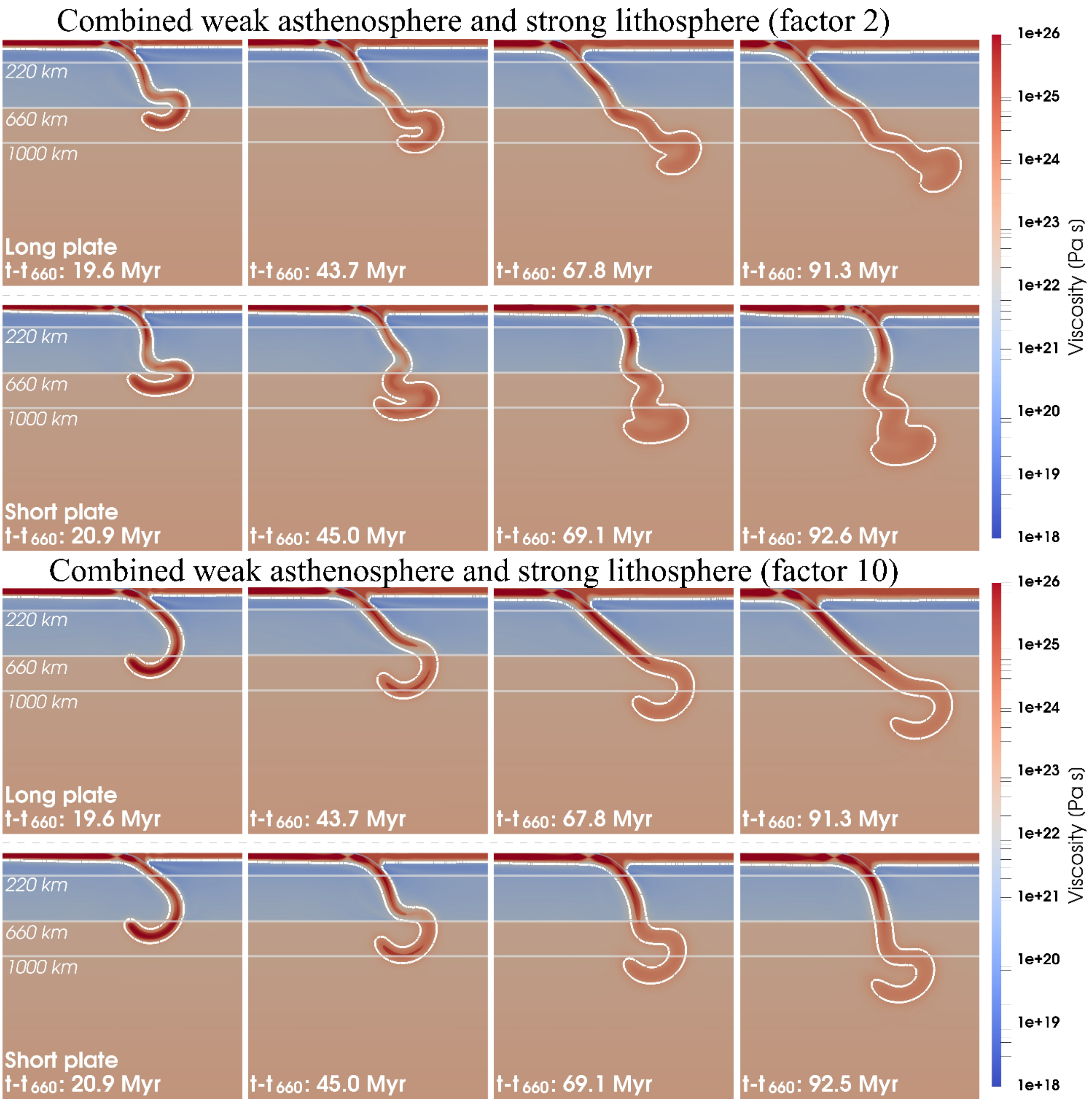

Figure S2-1 (continued)

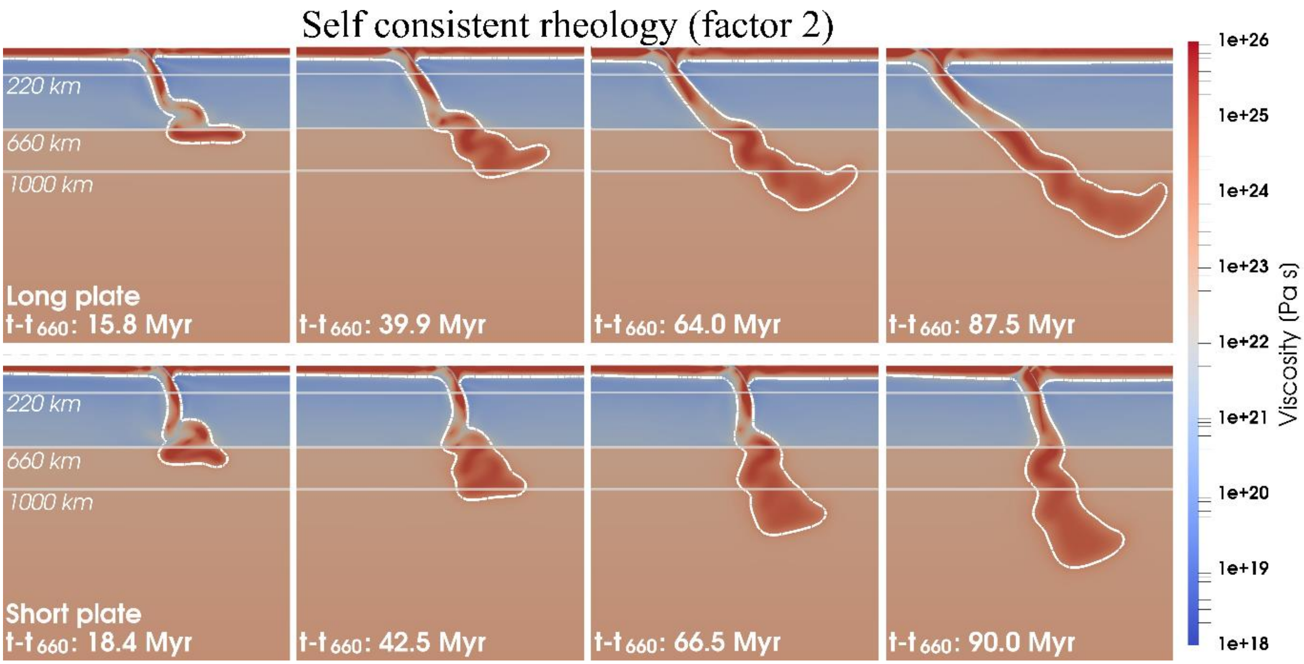

Figure S2-1 (continued)

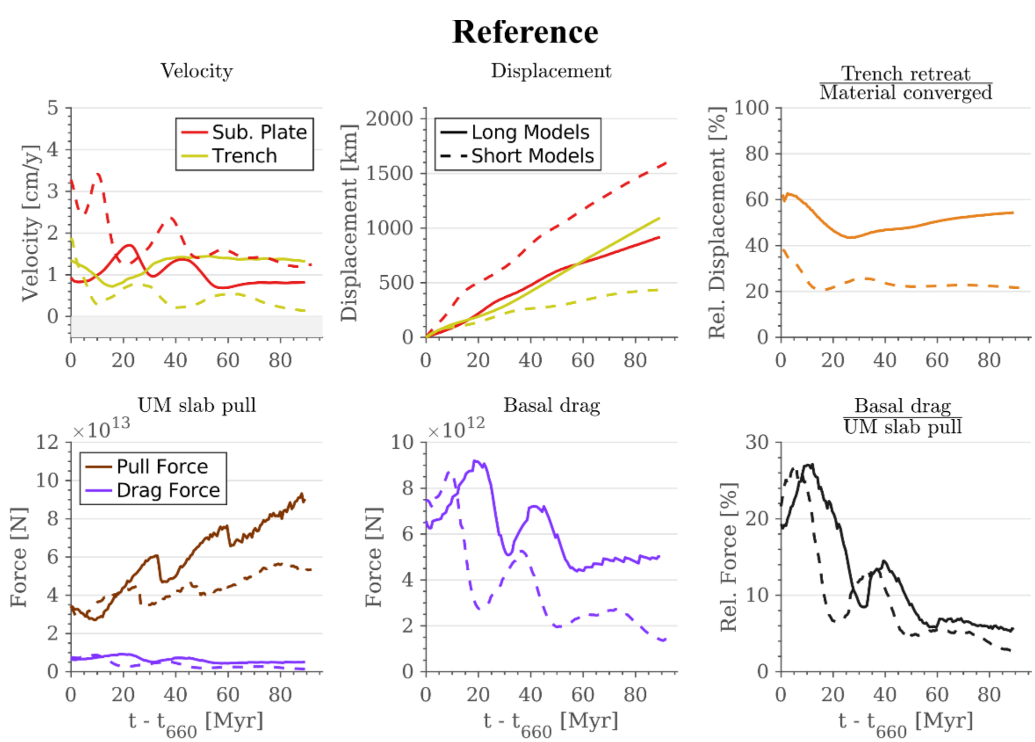

Figure S2-2: Temporal evolution, similar to Fig. 4, of the long-plate case (full lines) and the short-plate case (dashed lines) for all models. t-t660 indicates the time since the initial interaction of the slab with the ULMB. Panels show (from top left panel, along rows from top to bottom): (1) Velocity of the subducting plate (positive towards the upper plate, red) and the trench (positive away from the upper plate, yellow), measured at 2000 km distance from the initial subducting plate ridge (left hand boundary). (2) Displacement of the subducting plate (red) and the trench (yellow) relative to the initial condition. (3) Percent of plate convergence (calculated as the sum of trench retreat and plate displacement) achieved by trench retreat. (4) Upper-mantle slab pull and basal drag below the subducting plate, calculated as described in the main text. (5) Basal drag force from (4). (6) Ratio of basal drag to upper mantle slab pull force.

Weak asthenosphere

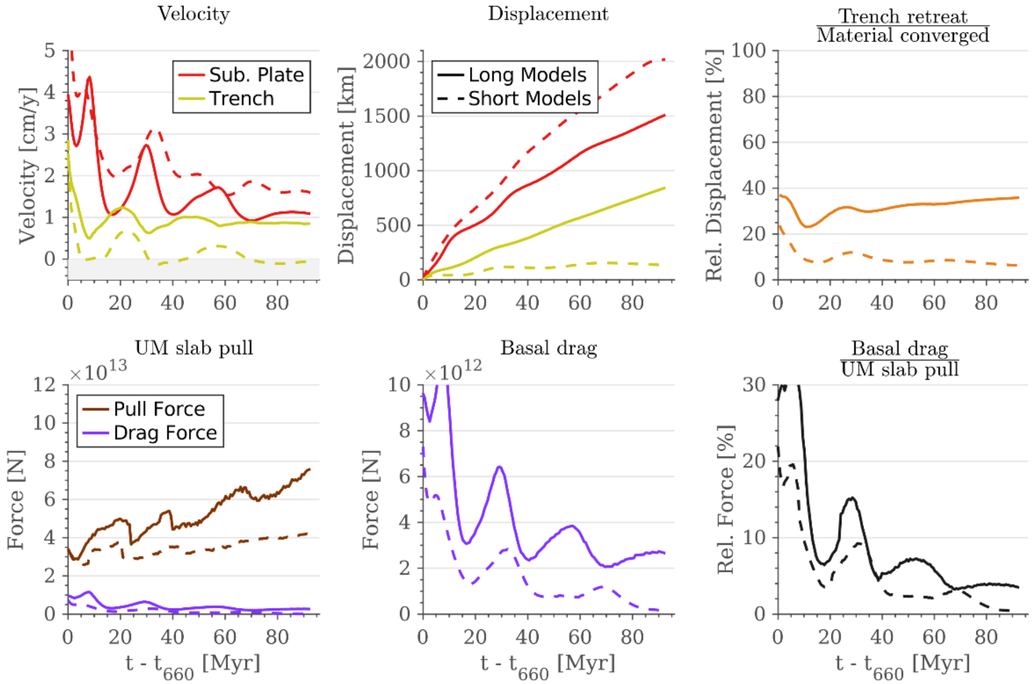

Strong lithosphere (factor 2)

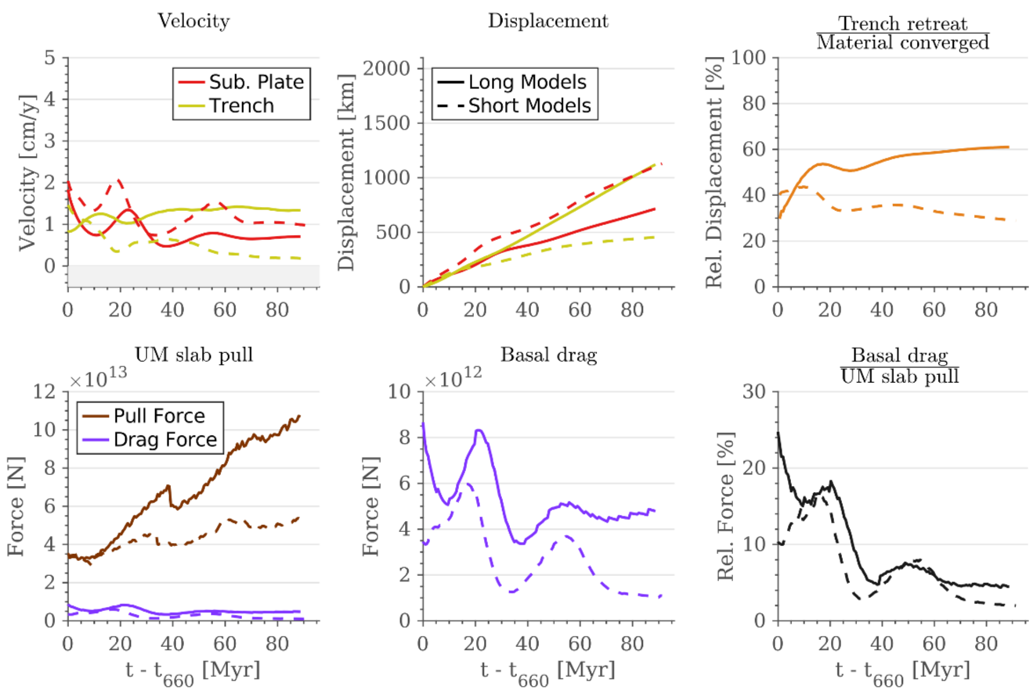

Figure S2-2 (continued)

Strong lithosphere (factor 10)

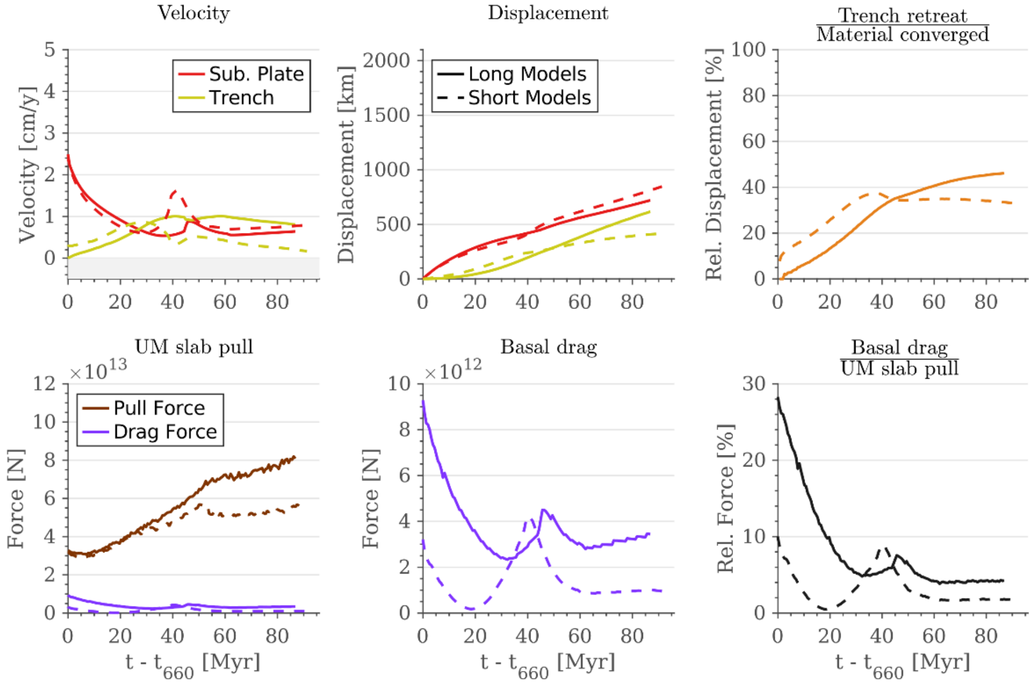

Combined weak asthenosphere and strong lithosphere (factor 2)

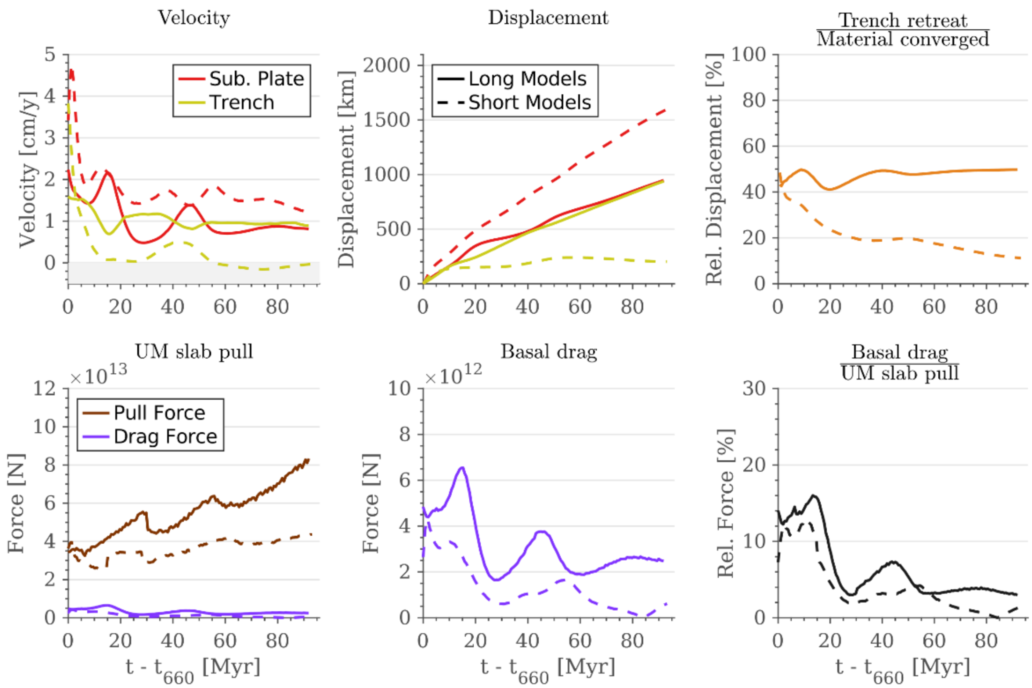

Figure S2-2 (continued)

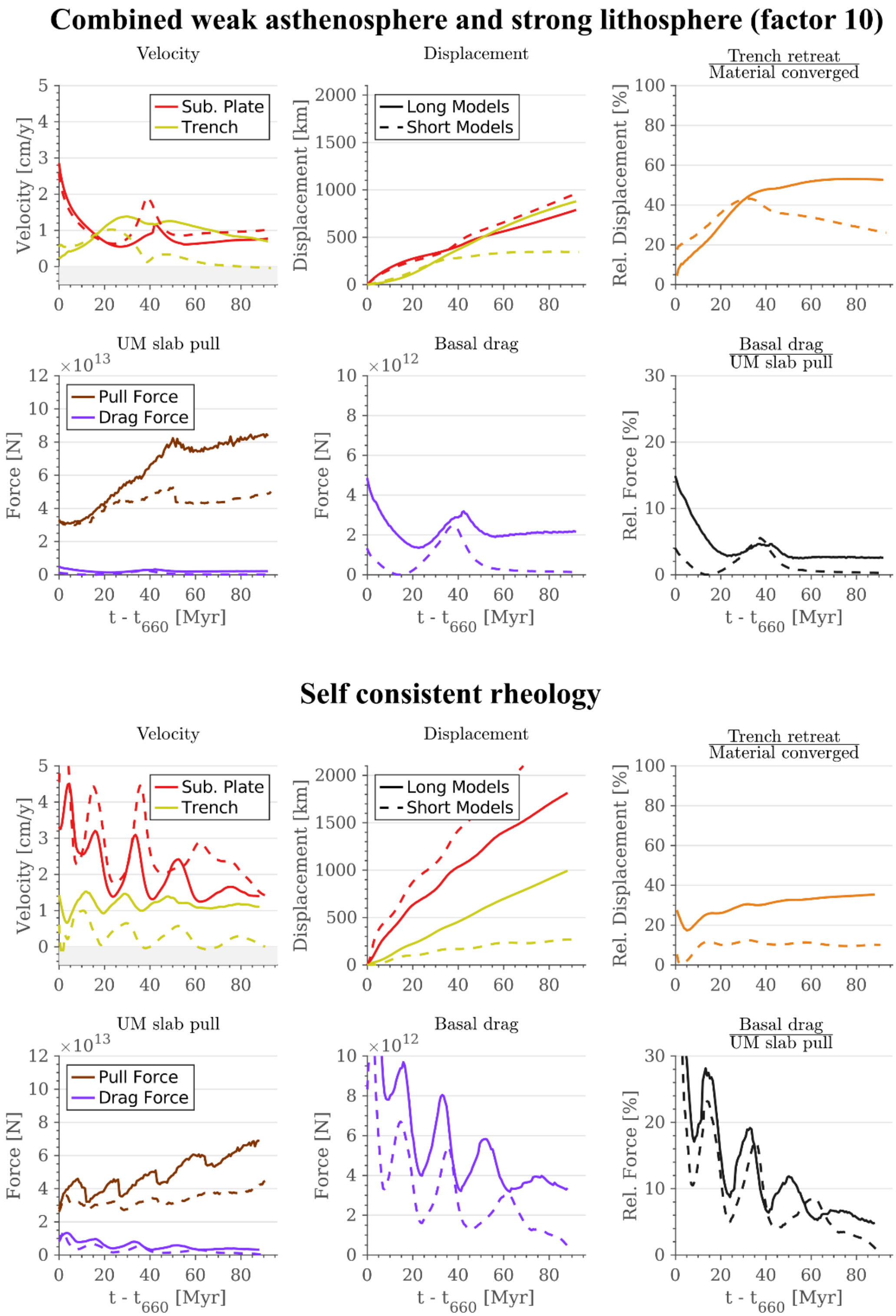

Figure S2-2 (continued)

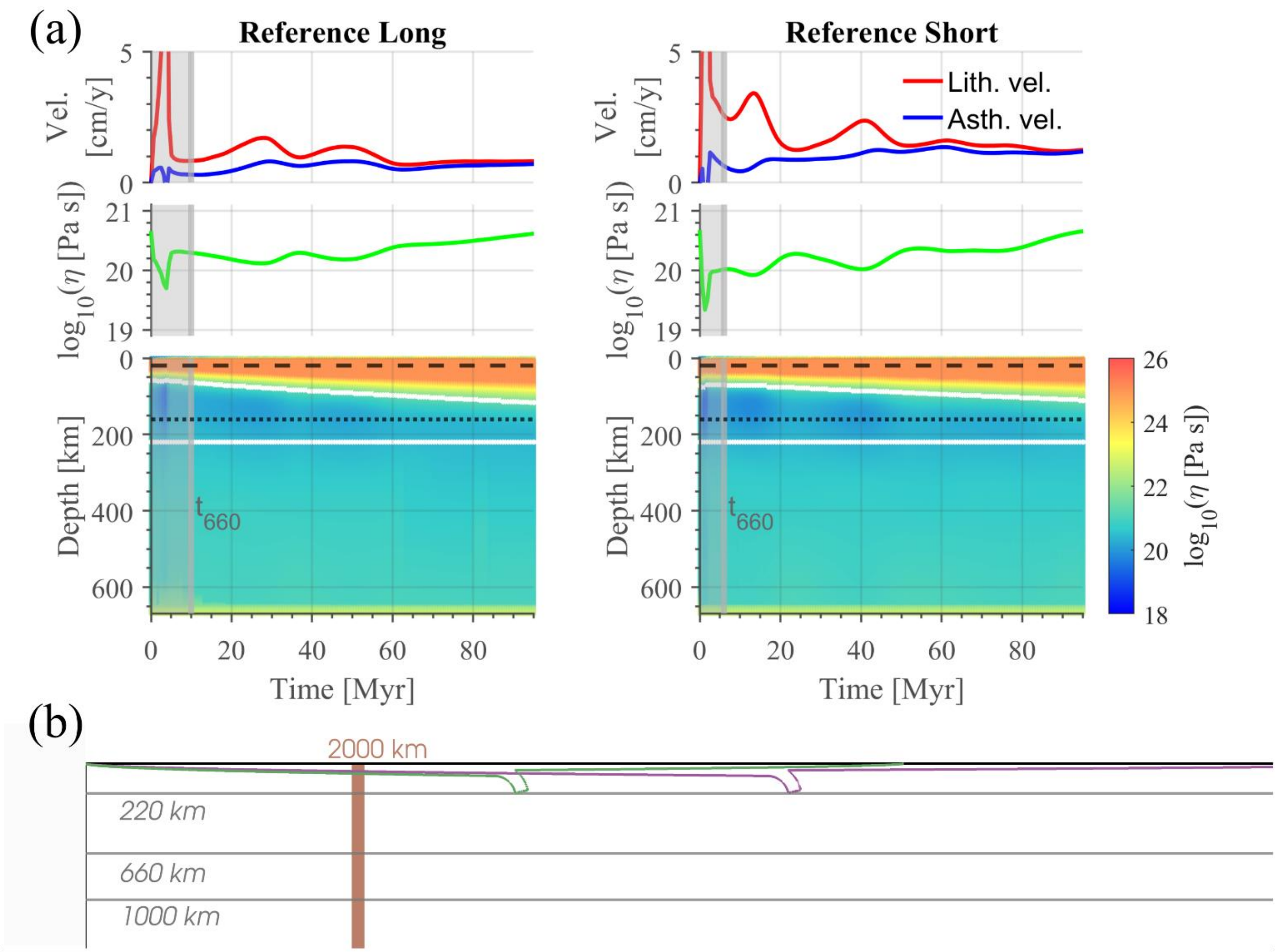

Figure S2-3 (a) Temporal evolution of parameters used for the calculation of basal drag (see main text for further details), for the long-plate reference model (left panels) and short-plate reference model (right panels). Top panel shows the velocities of the lithosphere (red line) and asthenosphere (blue line) (measured along the dashed and dotted lines in the bottom panel, respectively). Middle panel shows the magnitude of the viscosity of the asthenosphere (green line, measured along the dotted line in the bottom panel). Bottom panel shows a vertical profile (0-660 km depth) of the magnitude of the viscosity field. White lines mark the base of the lithosphere (1100°C isotherm) and asthenosphere (constant depth of 220 km). Parameters for the lithosphere were measured at 20 km depth (black dashed line) and parameters for the asthenosphere at 160 km depth (black dotted line). Time before the initial interaction of the slab with the ULMB, t660, is not shown in Fig. 4, 6 and 2.2 and shaded in this figure. (b) Location of the vertical profile location along which the quantities in (a) are measured (brown line), marked on an outline of the lithosphere at the initial condition of the long-plate reference model (magenta line) and the short-plate reference model (green line). The vertical and horizontal spatial scales are identical and only part of the full model domain is shown. Grey lines mark 220 km, 660 km (ULMB) and 1000 km depth.

S3. Cenozoic subduction zone parameters

We used GPlates (Müller et al., 2018) with the plate reconstruction of Müller et al. (2016) to make an updated compilation of the average velocities, average age at the trench and size of the subducting plates for major subduction zones through the Cenozoic (0-60 Ma). This was done for all trenches previously studied by Sdrolias and Müller (2006) who considered the Andean subduction zone, Central-North Farallon subduction systems, subduction below Alaska and the Aleutians, subduction below Japan-Kuriles-Kamchatka, subduction below Izu-Bonin-Marianas, below Tonga-Kermadec and below the Sunda-Banda arc. To these we added the subduction of the Philippine Sea plate and the final stages of the subduction of the Izanagi and Kula plates. In processing this database, we considered all the Pacific subduction systems (i.e. Alaska-Aleutians, Japan-Kuriles-Kamchatka, Izu-Bonin-Marianas and Tonga-Kermadec) as a single Pacific system.

The relevant trenches were identified by extracting the global subducted segments of all plate polygons in GPlates. All trenches were sampled at 50 km intervals, and the coordinates were output and then plotted to select those belonging to the major subducting plate systems listed above. For each selected system, age and velocities along the trench were plotted every 10 Myr to check that all data made sense, and to remove edge points where these were clearly anomalous from the rest of the trench (e.g. because of an anomalous age or convergence direction). We evaluated the point velocity of the subducting plate, of the overriding plate as well as convergence velocity and direction to select the segments to analyse. Maps showing the trench segments included in our analysis at each stage can be found in Fig. S3-1, where the sampling points along the trenches are also coloured according to the subducting plate absolute velocity (in the moving hotspot reference frame of O'Neill et al., 2005) and age. These maps illustrate the evolving set of subduction systems through the Cenozoic as well as the variability of age and velocity along each trench. Aside from some edge points, we excluded from our analysis the part of the South American trench at 40 and 50 Myr which was south of the Antarctic ridge and the Cocos subduction system at 20 Ma, because according to the plate motion model there is limited convergence along most of the trench at this time. Finally, we considered for our analysis the mean value of the velocities and trench age for each subducting system, and the standard variation of the mean value as the uncertainty.

There is some variation of both velocity and age along each trench, and each trench has a unique tectonic evolution. Nonetheless, the lack of a trend between velocity and size and the overall correlation between size and age are general features of the Cenozoic set of subduction zones, not dependent on including or excluding one or the other system, or on different definitions of each system, or on consideration of the total subducting plate velocity or only the normal component of velocity.Figure S3-1: Evolution of velocities and ages along the trenches considered in the global analysis of Cenozoic subduction systems, in intervals of 10 Myr. 3 maps are shown for each time interval, displaying the trenches used for the analysis (left), absolute subducting plate velocity in hotspot reference frame (O'Neill et al., 2005; middle) and age at the trench (right). Grey lines represent other boundaries of the subducting plates. The background light grey shows present day global coastlines for reference. Data is based on Müller et al. (2016) and processed using GPlates and Cartopy (Met Office, 2015; Müller et al., 2018).

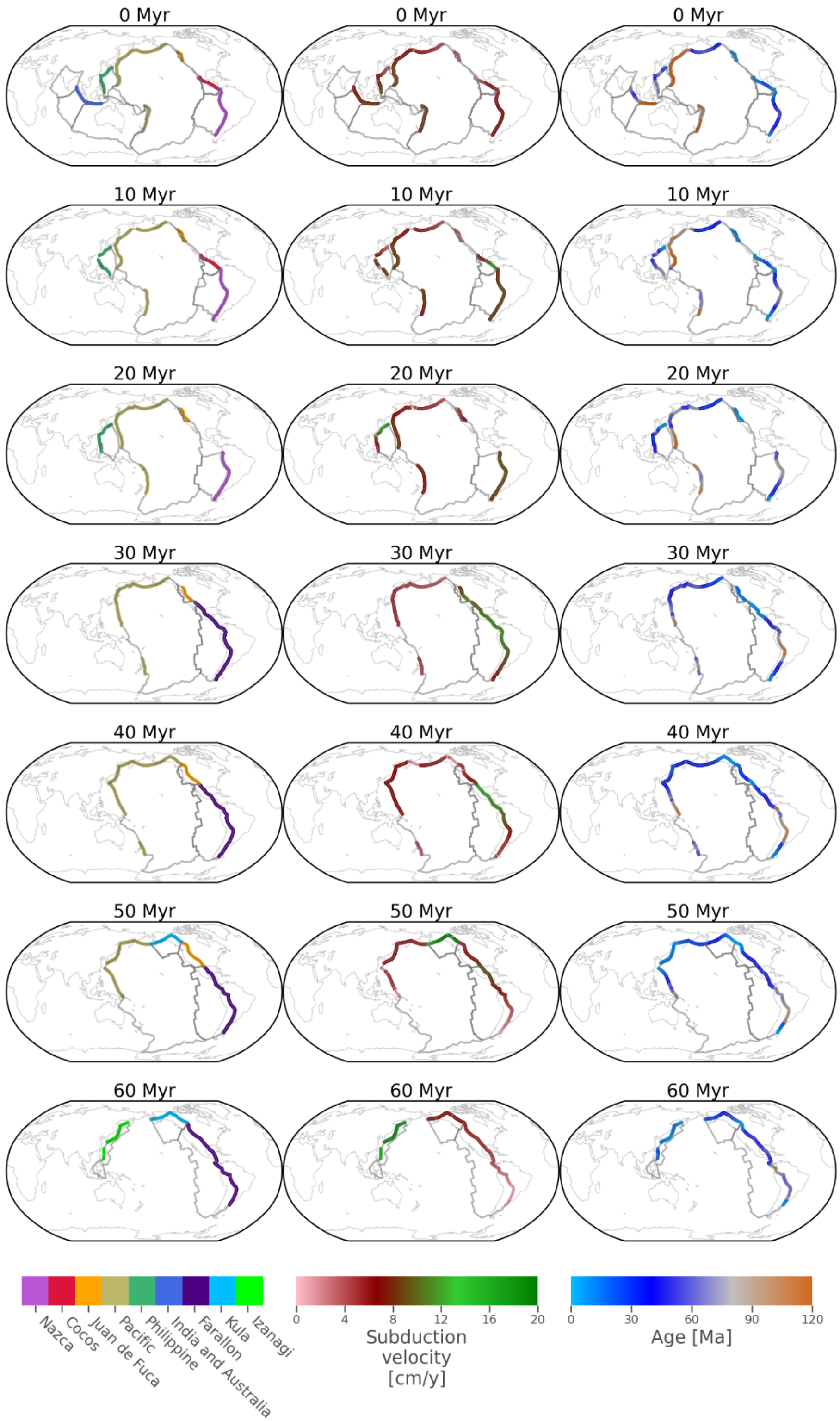

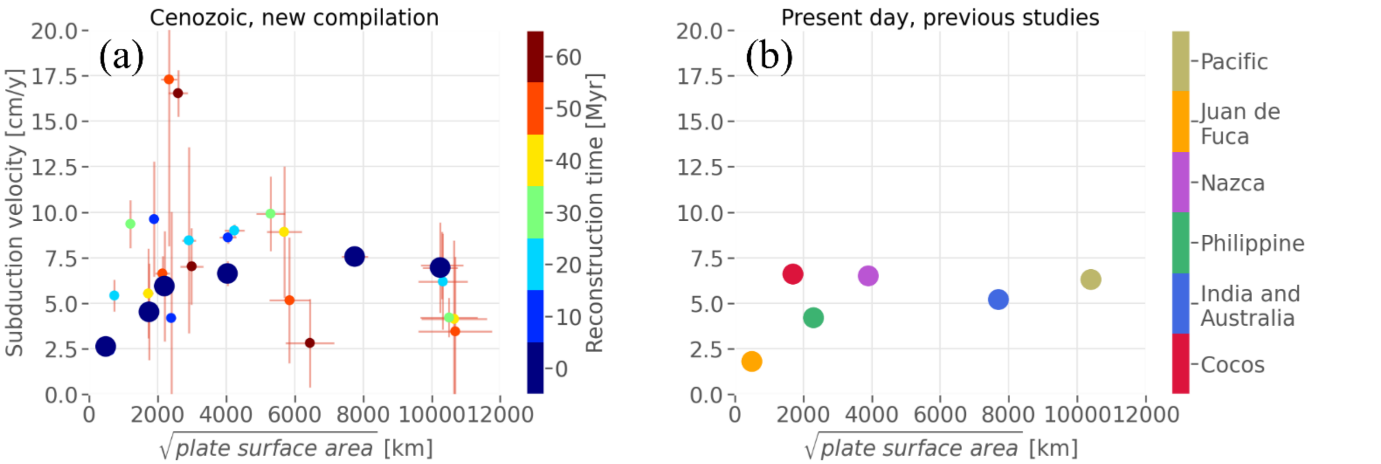

Figure S3-2: Velocity of subducting plates as a function of plate size. Plate size as typical length is calculated as the square root of the surface area of the plate. (a) Cenozoic dataset is based on plate reconstruction from Müller et al. (2016) and analysed using GPlates (Müller et al., 2018). Large markers indicate present day values from this reconstruction. (b) Present day velocities from Schellart et al. (2007) and Sdrolias and Müller (2006), as a function of plate size from Conrad and Hager (1999), same as shown in Fig. 1. All velocities are calculated in lower mantle (plume) reference frame (O'Neill et al., 2005).

References

Fowler, C. (2005), The Solid Earth: An Introduction to Global Geophysics, Cambridge Univ. Press, Cambridge, U. K.

Garel, F., Goes, S., Davies, D. R., Davies, J. H., Kramer, S. C. and Wilson, C. R.: Interaction of subducted slabs with the mantle transition-zone: A regime diagram from 2-D thermo-mechanical models with a mobile trench and an overriding plate, Geochemistry, Geophys. Geosystems, 15, 1739–1765, https://doi.org/10.1002/2014GC005257, 2014.

Hirth, G., and Kohlstedt, D. L.: Experimental constraints on the dynamics of the partially molten upper mantle: Deformation in the diffusion creep regime, J. Geophys. Res., 100, 1981–2001, https://doi.org/10.1029/94JB02128, 1995.

Hirth, G., and Kohlstedt, D. L.: Rheology of the Upper Mantle and the Mantle Wedge: A View from the Experimentalists, Geophys. Monogr. Ser., 138, 83–106, https://doi.org/10.1029/138GM06, 2003.

Karato, S., and Wu P.: Rheology of the upper mantle: A synthesis, Science, 260, 771–778, https://doi.org/10.1126/science.260.5109.771, 1993.

Korenaga, J. and Karato, S. I.: A new analysis of experimental data on olivine rheology, J. Geophys. Res.-Sol. Ea., 113, B02403, https://doi.org/10.1029/2007JB005100, 2008.

Maunder, B., van Hunen, J., Magni, V. and Bouilhol, P.: Relamination of mafic subducting crust throughout Earth's history, Earth Planet. Sci. Lett., 449, 206–216, https://doi.org/10.1016/j.epsl.2016.05.042, 2016.

Met Office: Cartopy: a cartographic python library with a Matplotlib interface, Available at: https://scitools.org.uk/cartopy, 2015.

Müller, R. D., Seton, M., Zahirovic, S., Williams, S. E., Matthews, K. J., Wright, N. M., Shephard, G. E., Maloney, K. T., Barnett-Moore, N., Hosseinpour, M., Bower, D. J. and Cannon, J.: Ocean Basin Evolution and Global-Scale Plate Reorganization Events Since Pangea Breakup, Annu. Rev. Earth Planet. Sci., 44(1), 107–138, https://doi.org/10.1146/annurev-earth-060115-012211, 2016.

Müller, R. D., Cannon, J., Qin, X., Watson, R. J., Gurnis, M., Williams, S., Pfaffelmoser, T., Seton, M., Russell, S. H. J. and Zahirovic, S.: GPlates: Building a Virtual Earth Through Deep Time, Geochemistry, Geophys. Geosystems, 19(7), 2243–2261, https://doi.org/10.1029/2018GC007584, 2018.

O'Neill, C., Müller, D., and Steinberger, B.: On the uncertainties in hot spot reconstructions and the significance of moving hot spot reference frames, Geochem. Geophys. Geosys., 6, Q04003, https://doi.org/10.1029/2004GC000784, 2005.

Ranalli, G.: Rheology of the earth, Chapman and Hall, London, ISBN 0-412-54670-1, 1995

Schellart, W. P., Freeman, J., Stegman, D. R., Moresi, L. and May, D.: Evolution and diversity of subduction zones controlled by slab width, Nature, 446(7133), 308–311, https://doi.org/10.1038/nature05615, 2007.

Sdrolias, M. and Müller, R. D.: Controls on back-arc basin formation, Geochem. Geophys. Geosys., 7, Q04016, https://doi.org/10.1029/2005GC001090, 2006.

Turcotte, D. L. and Schubert, G.: Geodynamics, 2nd ed., Cambridge University Press, Cambridge. https://doi.org/10.1017/CBO9780511807442, 2002.